

Several previous works (Kom Samo and Roberts, 2015; Remes et al., 2017, 2018) have attempted to further enhance the flexibility of spectral mixture kernels, such as the introduction of a time-dependent spectrum. However, we postulate that the key limitation in the SM kernel’s performance lies not its stationarity or expressivity, but in the optimisation procedure. We show that the form of the SM kernel gives rise to multiple symmetric modes in the marginal likelihood making optimisation extremely unstable and prone to overfitting.

Below we provide a summary of our main contributions:

- Highlight the failure modes of ML-II training in the context of spectral mixture kernels. We provide insights into the effectiveness of ML-II training in weak and strong data regimes.
- Demonstrate the practical feasibility of Hamiltonian Monte Carlo (HMC) / NUTS to sample from the hyperparameter space of the spectral mixture kernel class.
- Present the first demonstration of Nested Sampling (NS) as a means of sampling from the hyperparameter posterior, and its capability of identifying multiple modes.
- We demonstrate that in several time series modelling tasks, (where we predict the future given past observations) incorporating hyperparameter uncertainty yields superior prediction intervals.

Although this work focuses on the SM kernel class, many of the insights and general methodology are applicable to many other kernels used in the context of Gaussian process regression.

2 BACKGROUND

This section provides a brief account of marginalised Gaussian process regression, followed by an outline of the spectral mixture kernel (Wilson and Adams, 2013) which will be used in the numerical experiments.

2.1 Marginalised Gaussian Processes

Given some input-output pairs $(X, \mathbf{y}) = \{\mathbf{x}_i, y_i\}_{i=1}^N$ where y_i are noisy realizations of latent function values f_i with Gaussian noise, $y_i = f_i + \epsilon_i$, $\epsilon_i \sim \mathcal{N}(0, \sigma_n^2)$, we seek to infer some as-yet unseen values \mathbf{y}^* . Let $k_\theta(\mathbf{x}_i, \mathbf{x}_j)$ denote a positive definite kernel function parameterized with hyperparameters θ . Following the prescription of Lalchand and Rasmussen (2020), the

marginalised GP framework is given by

$$\begin{aligned} \text{Hyperprior: } & \theta \sim p(\theta), \\ \text{GP Prior: } & \mathbf{f}|X, \theta \sim \mathcal{N}(\mathbf{0}, K_\theta), \\ \text{Likelihood: } & \mathbf{y}|\mathbf{f} \sim \mathcal{N}(\mathbf{f}, \sigma_n^2 \mathbb{I}) \end{aligned} \quad (1)$$

where K_θ denotes the $N \times N$ covariance matrix, $(K_\theta)_{i,j} = k_\theta(\mathbf{x}_i, \mathbf{x}_j)$. The predictive distribution for unknown test inputs X^* integrates over the joint posterior¹,

$$p(\mathbf{f}^*|\mathbf{y}) = \iint p(\mathbf{f}^*|\mathbf{f}, \theta)p(\mathbf{f}|\theta, \mathbf{y})p(\theta|\mathbf{y})d\mathbf{f}d\theta \quad (2)$$

For Gaussian noise, \mathbf{f} can be treated analytically as follows

$$\begin{aligned} p(\mathbf{f}^*|\mathbf{y}) &= \int p(\mathbf{f}^*|\mathbf{y}, \theta)p(\theta|\mathbf{y})d\theta, \\ &\simeq \frac{1}{M} \sum_{j=1}^M p(\mathbf{f}^*|\mathbf{y}, \theta_j) = \frac{1}{M} \sum_{j=1}^M \mathcal{N}(\mu_j^*, \Sigma_j^*), \end{aligned} \quad (3)$$

where θ is dealt with numerically and θ_j correspond to draws from the hyperparameter posterior $p(\theta|\mathbf{y})$. The distribution inside the summation represents the standard GP posterior predictive for a fixed hyperparameter setting θ_j . Thus, the final form of the posterior predictive in marginalised GPs is a mixture of Gaussians (see Rasmussen and Williams (2006) for a review of GPs). Throughout this work we shall adopt a Gaussian likelihood, hence the only intractable integrand we need to consider is the hyperparameter posterior $p(\theta|\mathbf{y})$,

$$p(\theta|\mathbf{y}) \propto p(\mathbf{y}|\theta)p(\theta) \quad (4)$$

For non-Gaussian likelihoods, one would have to approximate the joint posterior over \mathbf{f} and θ .

In related work, Filippone and Girolami (2014) compared a range of MCMC algorithms for marginalised Gaussian processes. Murray and Adams (2010) used a slice sampling scheme for general likelihoods specifically addressing the coupling between \mathbf{f} and θ . Titsias and Lázaro-Gredilla (2014) presented an approximation scheme using variational inference. More recently, Lalchand and Rasmussen (2020) demonstrate marginalisation with HMC and variational inference.

2.2 Spectral Mixture Kernels

The spectral mixture kernel is characterised by a spectral density $S(\nu)$, defined as a mixture of Q Gaussian pairs (Wilson and Adams, 2013):

$$S(\nu) = \sum_{i=1}^Q \frac{w_i}{2} [G(\nu, \mu_i, \sigma_i) + G(\nu, -\mu_i, \sigma_i)]. \quad (5)$$

¹where we implicitly condition over inputs X, X^* for compactness.

Here the weight w_i specifies the variance contributed by the i th component while $G(\nu, \mu, \sigma)$ denotes a Gaussian function with mean μ_i and standard deviation σ_i . To avoid confusion with other standard deviations, and convey its physical significance, we shall refer to σ_i as the *bandwidth*.

The formalism of (5) is readily expanded to higher dimensions. If the power spectrum is represented by a sum of multivariate Gaussians, each with a diagonal covariance, with entries collected in the D dimensional vector σ_i , the corresponding kernel $k(\tau = \mathbf{x} - \mathbf{x}')$ takes the form,

$$k(\boldsymbol{\tau}) = \sum_{i=1}^Q w_i \cos(2\pi\boldsymbol{\tau} \cdot \boldsymbol{\mu}_i) \prod_{d=1}^D \exp(-2\pi^2 \tau_d^2 \sigma_i^{2(d)}) \quad (6)$$

where $\tau_d, \mu_i^{(d)}, \sigma_i^{(d)}$ are the d^{th} elements of the D dimensional vectors $\boldsymbol{\tau}, \boldsymbol{\mu}_i$ and $\boldsymbol{\sigma}_i$ respectively. The vector of kernel hyperparameters $\boldsymbol{\theta} = \{w_i, \boldsymbol{\mu}_i, \boldsymbol{\sigma}_i\}_{i=1}^Q$ is typically unknown, we account for this uncertainty by treating them as random variables.

Fig. 1 shows the marginal likelihood surface for a 2-component SM kernel, given two datasets of different size. One of the striking features of these surfaces lies in their symmetry: this is due to the kernel’s invariance to the ordering of its components. The marginal likelihood of a SM kernel with Q spectral components possesses $Q!$ identical regions of parameter space. A naive attempt to explore the full posterior distribution of a spectral mixture kernel would try to quantify probability mass across these degenerate regions, a much more computationally intensive task than is necessary. One solution is to only sample from one region, and ignore its symmetric counterparts. To achieve this, we can adopt an approach known as forced identifiability (Buscicchio et al., 2019) to ensure that the components are defined in sequential order with respect to their frequency μ .

3 CANDIDATE INFERENCE METHODS

This section summarises the three inference methods we wish to compare, starting with the *de facto* training method ML-II, followed by two sampling techniques: Hamiltonian Monte Carlo (HMC) and Nested Sampling (NS).

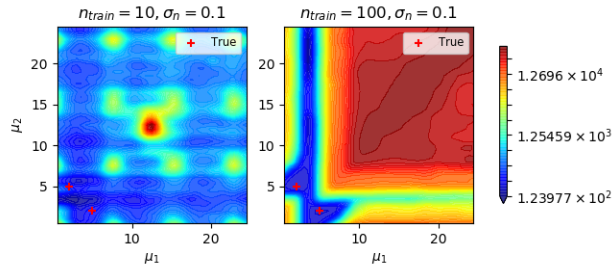


Figure 1: Visualising the negative log marginal likelihood surface as a function of mean frequencies in a 2 component spectral mixture kernel GP. The training data was generated from latent functions evaluated on the input domain $[-1,1]$ and σ_n refers to the intrinsic data noise level. The two identical peaks correspond to different re-orderings of the 2 component mean frequency vector with a true value of $[2,5]$.

3.1 ML-II

A Gaussian noise setting facilitates an analytically tractable marginal likelihood,

$$p(\mathbf{y}|\boldsymbol{\theta}) = \int p(\mathbf{y}|\mathbf{f})p(\mathbf{f}|\boldsymbol{\theta})d\mathbf{f} = \int \mathcal{N}(\mathbf{0}, K_{\boldsymbol{\theta}})\mathcal{N}(\mathbf{f}, \sigma_n^2\mathbb{I})d\mathbf{f} = \mathcal{N}(\mathbf{0}, K_{\boldsymbol{\theta}} + \sigma_n^2\mathbb{I}), \quad (7)$$

using the definitions from (1). ML-II estimates are obtained by maximizing $\mathcal{L}(\boldsymbol{\theta}) = \log p(\mathbf{y}|\boldsymbol{\theta})$ over the kernel hyperparameters, $\boldsymbol{\theta}_{\star} = \arg\max_{\boldsymbol{\theta}} \mathcal{L}(\boldsymbol{\theta})$.

Note that since the objective $\mathcal{L}(\boldsymbol{\theta})$ is the log marginal likelihood (where \mathbf{f} has been marginalised out), the procedure is called Type-II maximum likelihood (ML-II). This serves as our benchmark to compare against the marginalised version of training under two different sampling schemes.

Fig. 1 shows a two-dimensional slice of the 7-dimensional² negative log marginal likelihood surface corresponding to a SM kernel with 2 components. We can see that even with a 10 fold data increase, the flat ridge on the surface implies that gradient based optimisation might end up trapped in a bad local optima. Further, with small data sets the peaks are not pronounced enough and there is significant probability mass in regions of the hyperparameter space away from the true values.

3.2 Hamiltonian Monte Carlo (HMC)

Hamiltonian Monte Carlo (Duane et al., 1987) is a fundamental tool for inference in intractable Bayesian models. HMC relies on using gradient information to suppress random walk behaviour inherent to samplers

²A two component SM kernel has two weights, bandwidths and frequencies in addition to the noise level for a 1d dataset.

Algorithm 1: Nested Sampling for hyperparameter inference

Initialisation: Draw n_L ‘live’ points $\{\boldsymbol{\theta}\}_{i=1}^{n_L}$ from the prior $\boldsymbol{\theta}_i \sim \pi(\boldsymbol{\theta})$, set model evidence $\mathcal{Z} = 0$.

while *stopping criterion is unmet* **do**

- Compute $\psi_i = \min(\psi(\boldsymbol{\theta}_1), \dots, \psi(\boldsymbol{\theta}_N))$, the lowest marginal likelihood from the current set of live points.
- Sample a new live point $\boldsymbol{\theta}'$ subject to $\psi(\boldsymbol{\theta}') > \psi_i$
- Remove the point $\boldsymbol{\theta}_i$ corresponding to the lowest marginal likelihood ψ_i , moving it to a set of ‘saved’ points
- Assign estimated prior mass at this step $\hat{X}_i = e^{-\frac{i}{N}}$
- Assign a weight for the saved point, $V_i = \hat{X}_{i-1} - \hat{X}_i$
- Accumulate evidence, $\mathcal{Z} = \mathcal{Z} + \psi_i V_i$
- Evaluate stopping criterion, if triggered then break;

end

Add final n_L points to the ‘saved’ list of K samples:

- Weight of each of these final points is assigned to $p_i = \hat{X}_K / n_L \forall i = K, \dots, n_L + K$ // **final slab of enclosed prior mass**
- Final evidence is given by, $\mathcal{Z} = \sum_{i=1}^{n_L+K} \psi_i V_i$
- Importance weights for each sample are given by, $p_i = \psi_i V_i / \mathcal{Z}$

return *set of samples* $\{\boldsymbol{\theta}_i\}_{i=1}^{n_L+K}$, *along with importance weights* $\{p_i\}_{i=1}^{n_L+K}$ *and evidence estimate* \mathcal{Z} .

like Metropolis-Hastings and its variants. The sampler operates in an augmented space $(\boldsymbol{\theta}, \mathbf{p})$ of position variables and momentum variables where the position variables are the variable of interest. The momentum variables are sampled from an independent $\mathcal{N}(0, 1)$ and can safely be marginalised out from the joint samples to obtain just the samples of interest. New proposals are generated by simulating Hamiltonian dynamics in the joint 2D phase space $(\boldsymbol{\theta}_i, \mathbf{p}_i) \rightarrow (\boldsymbol{\theta}_{i+1}, \mathbf{p}_{i+1})$ (where D is the dimensionality of $\boldsymbol{\theta}$) for preset number of steps called the path length (L). Hamiltonian dynamics are simulated using the leap-frog symplectic integrator which relies on a step size (ϵ). Further, each iteration requires the gradients of the log marginal likelihood w.r.t the hyperparameters. In the case of a GP, this means each iteration of the leap-frog integrator requires the inversion of K_θ , L times to simulate one proposal. Refer to Neal et al. (2011) for a detailed tutorial. In the experiments we use a self-tuning variant of HMC called the No-U-Turn Sampler (NUTS) (Hoffman and Gelman, 2014) where the path length is adapted for every iteration. NUTS is frequently shown to work as well as a hand-tuned HMC; hence in this way we avoid the compute overhead in tuning for good values of the step-size (ϵ) and path length (L). We use the version of NUTS available in the python package `pymc3`.

3.3 Nested Sampling

The nested sampling algorithm was developed by Skilling (2004) (see also Skilling et al. (2006)) as a means of estimating the model evidence $\mathcal{Z} = \int \psi(\boldsymbol{\theta}) d\boldsymbol{\theta}$, where ψ denotes the likelihood, and $p(\boldsymbol{\theta})$ the prior.

This may be recast as a one-dimensional integral over the unit interval, $\mathcal{Z} = \int_0^1 \psi(X) dX$, irrespective of the dimensionality of $\boldsymbol{\theta}$. Here X is the quantile function associated with the likelihood: it describes the volume of the prior lying below the likelihood value ψ . The extreme values of the integrand, $\psi(X=0)$ and $\psi(X=1)$, therefore correspond to the minimum and maximum likelihood values found under the support of the prior $\pi(\boldsymbol{\theta})$.

Sampling proceeds in accordance with Algorithm 1. While the sequence of samples provides an estimate of \mathcal{Z} , an invaluable quantity in the context of Bayesian model selection, they also represent importance weighted samples of the posterior.

If we wished to perform inference in a low-dimensional setting, then a uniform sampling strategy would suffice. However since we wish to explore higher dimensions, we employ the PolyChord algorithm (Handley et al., 2015; Handley et al., 2015), which performs slice sampling (Neal, 2003) at each iteration. Unless otherwise stated, we use 100 live points, which are bounded in a set of ellipsoids (Feroz et al., 2009). These bounding surfaces allow the macroscopic structure of the likelihood contours to be traced, enabling a much more efficient sampling process. This approach has proven particularly adept at navigating multi-modal likelihood surfaces (Allison and Dunkley, 2014). These attractive properties have motivated numerous scientific applications, including the detection of gravitational waves (Veitch et al., 2015), the categorisation of cosmic rays (Cholis et al., 2015), and the imaging of a supermassive black hole (Akiyama et al., 2019).

The algorithm described above is implemented as part of the DYNesty package (Speagle, 2020). We use the ‘rslice’ sampling option, along with the default number of five slices, and adopt the default criterion for convergence. This is defined as the point at which the estimated posterior mass contained within the set of live points falls below 1% of the total.

4 HYPERPRIORS FOR THE SPECTRAL MIXTURE PRIOR

In this section we outline a suitable set of priors for the three fundamental parameters of a single spectral component. As defined in (5), these are the mean frequency μ , bandwidth σ , and weight w . For most of these hyperparameters, we find it is sufficient to impose a weakly informative prior of the form $\{\sigma, w, \sigma_n^2\} \sim \text{LogNormal}(0, 2)$. However the spectral component’s characteristic frequency μ deserves closer attention.

Two properties of the data strongly influence our perspective on which frequencies we can expect to observe: the fundamental frequency and the highest observable frequency. The fundamental frequency ν_F is the lowest frequency observable within the data, and is given by the inverse of the interval spanned by the observed x locations. Meanwhile the maximum frequency ν_N represents the highest observable frequency. For gridded data, this is naturally determined by the Nyquist frequency, which is half the sampling frequency.

It is crucial to bear in mind that the spectral density we wish to model is that of the underlying process, and not the spectral density of the data. These two quantities are often very different, due to the limited scope of the observations. For example, the change in stock prices over the period of a single day cannot exhibit frequencies above 10^{-6}Hz . Yet the process will have received contributions from long term fluctuations, such as those due to macroeconomic factors, whose periods can span many years. If we make no assumption regarding the relationship between the process we wish to model and

the finite range over which it is observed, then a priori, some as-yet undiscovered frequency within the process ought to be considered equally likely to lie above or below the fundamental frequency. Furthermore, given the large initial uncertainty in frequency μ , it is appropriate to adopt a prior which spans many orders of magnitude.

Towards very low frequencies, $\mu \ll \nu_F$, a sinusoid contributes very little variance to the observations - an annual modulation makes a tiny contribution to a minute’s worth of data. As we consider frequencies much lower than the fundamental frequency, it therefore becomes less likely that we will detect their contributions. We model this suppressed probability of observation with a broad Gaussian in log frequency for the regime $\mu < \nu_F$. Meanwhile, at frequencies above the Nyquist frequency, $\mu > \nu_N$, we encounter a degenerate behaviour: these sinusoids are indistinguishable from their counterparts at lower frequencies: they are said to be aliases of each other. As a result of this aliasing behaviour, the likelihood surface is littered with degenerate modes with identical likelihood values. From a computational perspective, it is advantageous to restrict our frequency parameter to a much narrower range than is permitted by our prior, while maintaining the same probability mass. As illustrated in the supplementary, mapping these higher frequencies down to their corresponding alias at $\mu < \nu_N$ yields a uniform prior on μ .

$$\mu/\nu_F \sim \begin{cases} \text{Lognormal}(0, 7), & \text{for } \mu < \nu_F, \\ \text{Uniform}(1, \nu_N/\nu_F), & \text{for } \nu_F < \mu < \nu_N. \end{cases} \tag{8}$$

5 EXPERIMENTS

5.1 Synthetic data

As a first demonstration of how the different methods perform, we draw four samples from a two-component SM kernel with known weights, frequencies and band-

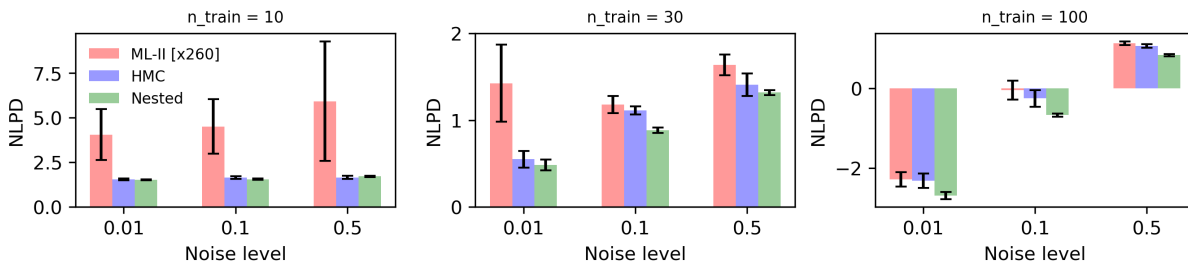


Figure 2: The impact of marginalising hyperparameters on the predictive performance (NLPD) of a spectral mixture kernel. The error bars at each noise level correspond to the mean NLPD and standard error of the mean across a diversity of latent functions. Nested sampling significantly outperforms ML-II in all nine experiments. The subplots contain the performance summaries under the different configurations. *Left*: Sparse distribution of training data ($n_{train} = 10$). *Middle*: Moderate sized distribution of training data ($n_{train} = 30$). *Right*: Dense distribution of training data ($n_{train} = 100$) - all on a fixed domain $[-1, +1]$.

widths. For each latent function sample we construct noisy training data across three noise levels $[0.01, 0.1, 0.5]$ and three training sizes $[10, 30, 100]$, on a fixed input domain $[-1, 1]$. In this way we seek to quantify the quality of predictions and prediction uncertainty under weakly identified regimes characterised by very few data points in a fixed domain to strongly identified regimes characterized by a dense distribution of data in a fixed domain. Further, the intrinsic noise level σ_n^2 of the data can also impact inference in weakly and strongly identified data regimes. In order to analyse the impact of σ_n^2 and training size we calculate the average performance across each of three different noise levels for each training set size.

We train under each of the candidate inference methods (ML-II, HMC, Nested) for each of the 9×4 data sets created and report prediction performance in terms of the average negative log predictive density (NLPD) for test data in Figure 2. ML-II uses five random restarts with a initialisation protocol tied to the training data. Following protocols from Wilson and Adams (2013), the SM weights (w_i) were initialised to the standard deviation of the targets \mathbf{y} scaled by the number of components ($Q = 2$). The SM bandwidths (σ_i) were initialised to points randomly drawn from a truncated Gaussian $|\mathcal{N}(0, \max d(x, x')^2)|$ where $\max d(x, x')$ is the maximum distance between two training points and mean frequencies (μ_i) were drawn from $\text{Unif}(0, \nu_N)$ to bound against degenerate frequencies. HMC used $\text{LogNormal}(0, 2)$ priors for all the hyperparameters. The ML-II experiments used `gpytorch` while the HMC experiments used the NUTS sampler in `pymc3`.

In Figure 2 we notice that ML-II struggles with small training data sets and catastrophically underestimates the noise level. The two sampling methods, HMC and NS, perform comparably well, though it is notable that a single NS run correctly identifies both modes in the likelihood surface, while a single HMC chain can only discover one.

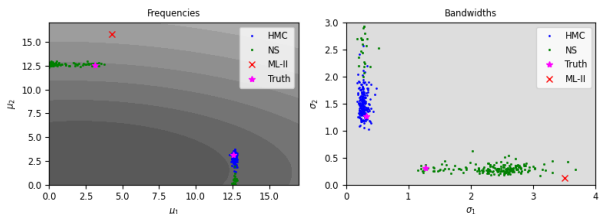


Figure 3: A comparison of hyperparameter estimation, where the ground truth is indicated by the magenta star. The grey shading indicates the prior. *Left:* Recovering the mean frequency parameters of the two spectral components. *Middle:* Recovering the two bandwidth parameters of the two spectral components. The true hyperparameters are $[\mu_1, \mu_2] = [3.14, 12.56]$ and $[\sigma_1, \sigma_2] = [1.27, 0.32]$. For frequencies and bandwidths we note the symmetry i.e. the estimates can converge on $[\mu_1, \mu_2]$ or $[\mu_2, \mu_1]$, and that the nested sampling algorithm successfully identifies both modes whereas HMC can only sample from one.

In Fig. 3 we summarise the performance of ML-II, HMC and nested sampling inference in their ability to recover the true setting of the hyperparameters for a synthetic dataset with 100 datapoints, a noise amplitude of $\sigma_n = 0.1$ and a signal-to-noise ratio of ≈ 3.2 on a fixed domain $[-1, 1]$. The magenta star \star denotes the true value and the red cross \times denotes the ML-II estimate. The HMC and NS sampling schemes are both better at recovering the ground truth hyperparameters than the point estimates. Further, the nested sampling scheme is able to obtain samples from both modes inherent in the marginal likelihood.

5.2 Time series benchmarks

For a more challenging test of our inference methods, we evaluate their predictive performance against thirteen realistic time series, as used in Lloyd et al. (2014)³. The time series are of variable length, with up to 1,000 data points in each. All models are trained on normalised data, but the quoted test performance is evaluated in the original space. The output is scaled to zero mean and unit variance, while the input space is scaled to span the unit interval, thereby ensuring $\nu_F = 1$. Given the complex nature of the task, we utilise more spectral components than for the synthetic case. Our fiducial kernel has seven components ($Q = 7$), yielding a 22-dimensional hyperparameter space to explore. For reference, we also include results from the Neural Kernel Network (Sun et al., 2018) where a flexible kernel is learnt incrementally through a weighted composition of primitive base kernels. This is trained with the Adam optimiser for 100,000 iterations and a learning rate of 10^{-3} .

In Table 1 we report the negative log of predictive density (NLPD) across test data. The evaluation was

³The raw data is available at <https://github.com/jamesrobertlloyd/gpss-research/tree/master/data/tsdlr-renamed>

Table 1: NLPD values for various GP methods across a range of time series tasks.

KERNEL	SPECTRAL	SPECTRAL	SPECTRAL	NKN
INFERENCE	ML-II	HMC	NESTED SAMPLING	ML-II
AIRLINE	7.25	5.83	5.22	5.6
BIRTHS	5.17	5.23	4.96	5.42
CALL CENTRE	11	7.32	7.29	7.76
GAS PRODUCTION	15.2	12.4	11	12.4
INTERNET	11.3	11.4	13.2	12.6
MAUNA	1.5	3.32	1.8	3.4
RADIO	2.19	2.12	2.07	4.12
SOLAR	1.4	0.82	0.58	2.38
SULPHURIC	5.13	5.15	5.11	6.32
TEMPERATURE	2.8	2.49	2.52	4.2
UNEMPLOYMENT	12.8	11.2	10.6	8.5
WAGES	159	8.71	6.59	4.28
WHEAT	8.47	6.44	6.58	6.24
MEAN	18.7	6.34	5.96	6.40
	± 1.2	± 0.03	± 0.03	

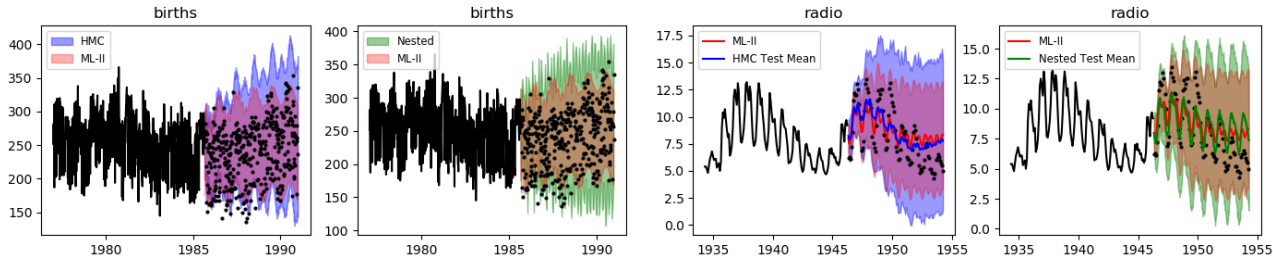


Figure 4: An illustration of the systematic underestimation of predictive uncertainty when adopting point estimates of kernel hyperparameters. Here we show 95% test confidence intervals derived from the spectral mixture kernel. Black lines denote training data and the black dots denote test data. *Left:* ‘BIRTHS’ data set - the ML-II intervals capture 84% of the test data where HMC and NS capture 93% and 99% of the test points respectively. *Right:* ‘RADIO’ data set (also showing test mean prediction) - the three methods show similar performance however, the average predictive density under test data is higher under the sampling methods.

conducted with a 60/40 train/test split.

The quoted uncertainties are estimated by repeating each set of experiment three times with a different random seed. We find that the spectral mixture kernel exhibits significant performance gains when using a sampling-based inference method compared to the conventional ML-II approach. HMC and NS offer similar performance levels, though NS carries an advantage of faster evaluation times and an estimate of the model evidence. More detailed results for various configurations of the nested sampler can be found in Table 2.

Fig. 5 is a zoomed in plot of the ‘RADIO’ predictions. It helps convey exactly why the NLPDs corresponding to the marginalised GP schemes are better. The left plot shows test predictions and respective 95% intervals. The blue band corresponds to prediction intervals under the marginalised HMC scheme; the 95% quantiles are estimated empirically by sampling from the Gaussian mixture distribution at each test input X^* . The right plot shows the mixture density for a single test point, the predictive mixture form places higher probability mass on the true test point than the narrower ML-II intervals.

Table 2: NLPD values for various configurations of the nested sampling algorithm.

	FIDUCIAL	DENSE	MULTI-RUN	PRIOR
LIVE POINTS	100	500	100	100
RUNS	1	1	5	1
PRIOR	LOG	LOG	LOG	UNIFORM
AIRLINE	5.36	4.66	5.36	8.88
BIRTHS	4.67	4.68	4.65	4.73
CALL CENTRE	6.54	6.17	6.45	6.46
GAS PRODUCTION	5.97	6.38	5.92	8.10
INTERNET	11.3	11.3	11.3	11.4
MAUNA	0.96	1.15	1.09	3.73
RADIO	1.95	2.03	1.84	2.19
SOLAR	-0.17	-0.20	-0.19	-0.28
SULPHURIC	5.42	5.58	5.15	6.07
TEMPERATURE	2.65	2.64	2.63	2.94
UNEMPLOYMENT	6.31	6.21	6.31	6.26
WAGES	2.19	2.24	2.20	1.97
WHEAT	4.97	5.20	5.39	5.42
MEAN	4.47 ±0.03	4.46 ±0.02	4.47 ±0.03	5.22 ±0.05

Fig. 6 depicts training times in wall clock seconds for our time-series experiments, all of which were run on a single Nvidia GTX1070 GPU. For HMC this corresponds to a single chain with 500 warm-up iterations and 500 samples. Nested sampling was performed with 100 live points, and the sampling continued until the convergence criterion was met.

Across these benchmarks, HMC was found to be slower by approximately a factor of two compared to nested sampling. Both methods could enjoy significant gains in speed with schemes such as those proposed in Loper et al. (2020).

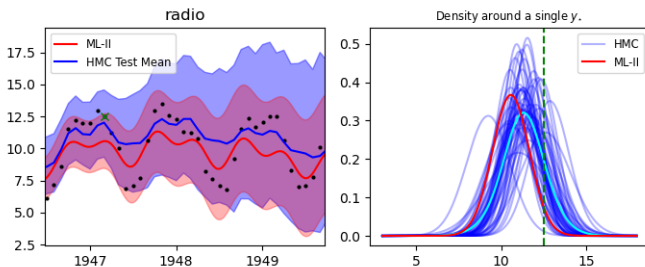


Figure 5: *Left:* Test means and 95% intervals, the green cross is the test point whose mixture density is enumerated on the right. *Right:* An illustration of how the predictive density is comprised of a mixture of Gaussians, yielding broader intervals and a correspondingly better NLPD.

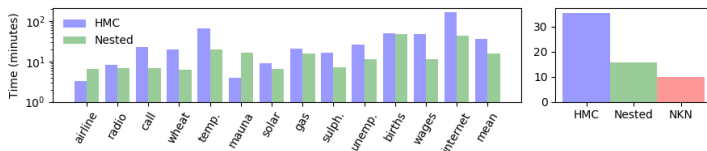


Figure 6: *Left:* Training time for each of the time series benchmarks. *Right:* Average training time (across data sets). It is interesting to note that nested sampling is only marginally more compute intensive than performing conventional ML-II inference with the neural kernel network.

5.3 2d Pattern Extrapolation

To provide a demonstration of how the inference methods are readily adapted to higher dimensional kernels, we revisit the challenge presented in Sun et al [26]. The two-dimensional ground truth function is given by $y = (\cos 2x_1 \times \cos 2x_2)\sqrt{|x_1x_2|}$. We train with just 50 points (as opposed to 100 in the original reference), which are chosen at random across $[-6, +6]$ in the xy -domain. The test points are defined on a 20×20 grid.

In Figure 7 we visualise the mean values of the posterior predictive distribution from three different inference methods: ML-II, HMC and nested sampling (NS). Visually, the reconstruction under the marginalised GP schemes (HMC / NS) appears to be superior to ML-II. Further, the 95% confidence intervals (not visualised) differ markedly, as is evident from the NLPD values. These are given by 216, 2.56, and 2.62 for ML-II, HMC and NS respectively (*lower* is better). For reference we also trained the neural kernel network (Sun et al [26]), which achieved an NLPD of 3.8.

This experiment marks a significant increase in the dimensionality of our parameters space, since in two dimensions each spectral component has five degrees of freedom. Yet the marginalised Gaussian processes comfortably outperform competing methods. ML-II was trained with Adam (learning rate=0.05) with 10 restarts and 2,000 iterations.

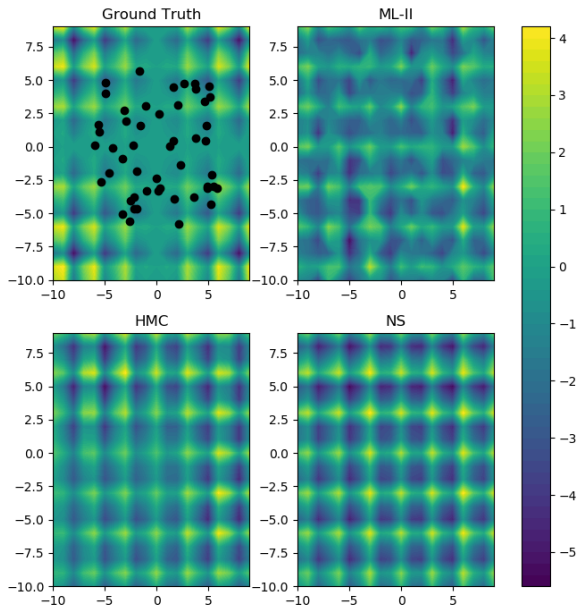


Figure 7: Learning a two-dimensional pattern with a 10 component spectral mixture kernel. *Top Left:* The ground truth, and the black dots denote the locations of the 50 training points. *Top Right:* Posterior predictive mean under ML-II. *Bottom Left:* Posterior predictive mean under HMC. *Bottom Right:* Posterior predictive mean under nested sampling.

6 DISCUSSION

We have performed the first demonstration of marginalised spectral mixture kernels, finding significant performance gains are readily available relative to the conventional approach of using point estimates for the hyperparameters. We also present the first application of nested sampling to Gaussian processes, a promising avenue given its inherent capability of exploring multimodal surfaces, especially since modern incarnations such as PolyChord (Handley et al., 2015) allow higher dimensional spaces to be explored.

The benefits of performing full GP marginalisation are three-fold. Firstly, it defends against overfitting of hyperparameters, which may occur when their uncertainty is substantial. Secondly, there is a lower susceptibility to getting trapped in sub-optimal local minima. Thirdly, they provide more robust prediction intervals by accounting for hyperparameter uncertainty. These three advantages become particularly pronounced when expressive kernels with several hyperparameters are used (such as the spectral mixture kernel), or where the training data is either sparse or noisy.

While a pathological marginal likelihood geometry can pose problems for both gradient based optimisation and sampling; sampling schemes are able to quantify them better if the practical difficulties of deploying them (like chains stuck in bad optima) are overcome. The nested sampling scheme, which does not require gradient information, provides an opportunity to sample the multimodal posterior at a fraction of the cost of running HMC. Further, it is crucial to ask if we are exploiting the full expressivity of kernels by resorting to point estimates as a summation of the learning exercise? A marginalised GP with a standard SM kernel not only improved upon its conventional counterpart, but also surpassed the performance of the Neural Kernel Network model (Sun et al., 2018) in the time series tasks, despite possessing far fewer hyperparameters. This shows that there is merit in the question.

The recent advancements in inference capabilities across MCMC and variational inference, in terms of both scale and accuracy, are bound to make such hierarchical models mainstream. The methods discussed here can seamlessly work in a sparse GP framework when dealing with large N . Future work will focus in this direction to make marginalised Gaussian process inference the norm rather than the expensive exception.

References

- Carl Edward Rasmussen and Christopher KI Williams. *Gaussian processes in machine learning*. Springer, 2006.
- Andrew Wilson and Ryan Adams. Gaussian process kernels for pattern discovery and extrapolation. In *International Conference on Machine Learning*, pages 1067–1075, 2013.
- Salomon Bochner. *Lectures on Fourier integrals*, volume 42. Princeton University Press, 1959.
- Yves-Laurent Kom Samo and Stephen Roberts. Generalized spectral kernels. *arXiv preprint arXiv:1506.02236*, 2015.
- Sami Remes, Markus Heinonen, and Samuel Kaski. Non-stationary spectral kernels. In *Advances in Neural Information Processing Systems*, pages 4642–4651, 2017.
- Sami Remes, Markus Heinonen, and Samuel Kaski. Neural non-stationary spectral kernel. *arXiv preprint arXiv:1811.10978*, 2018.
- Vidhi Lalchand and Carl Edward Rasmussen. Approximate inference for fully bayesian gaussian process regression. volume 118 of *Proceedings of Machine Learning Research*. PMLR, 08 Dec 2020.
- Maurizio Filippone and Mark Girolami. Pseudo-marginal Bayesian inference for Gaussian processes. *IEEE Transactions on Pattern Analysis and Machine Intelligence*, 36(11):2214–2226, 2014.
- Iain Murray and Ryan P Adams. Slice sampling covariance hyperparameters of latent gaussian models. In *Advances in neural information processing systems*, pages 1732–1740, 2010.
- Michalis Titsias and Miguel Lázaro-Gredilla. Doubly stochastic variational bayes for non-conjugate inference. In *International conference on machine learning*, pages 1971–1979, 2014.
- Riccardo Buscicchio, Elinore Roebber, Janna M. Goldstein, and Christopher J. Moore. Label switching problem in bayesian analysis for gravitational wave astronomy. *Physical Review D*, 100(8), Oct 2019. ISSN 2470-0029. doi: 10.1103/physrevd.100.084041. URL <http://dx.doi.org/10.1103/PhysRevD.100.084041>.
- Simon Duane, Anthony D Kennedy, Brian J Pendleton, and Duncan Roweth. Hybrid monte carlo. *Physics letters B*, 195(2):216–222, 1987.
- Radford M Neal et al. MCMC using hamiltonian dynamics. *Handbook of Markov chain Monte Carlo*, 2(11):2, 2011.
- Matthew D Hoffman and Andrew Gelman. The No-U-Turn sampler: adaptively setting path lengths in Hamiltonian Monte Carlo. *Journal of Machine Learning Research*, 15(1):1593–1623, 2014.
- John Skilling. Nested Sampling. In Rainer Fischer, Roland Preuss, and Udo Von Toussaint, editors, *American Institute of Physics Conference Series*, volume 735 of *American Institute of Physics Conference Series*, pages 395–405, November 2004. doi: 10.1063/1.1835238.
- John Skilling et al. Nested sampling for general bayesian computation. *Bayesian analysis*, 1(4):833–859, 2006.
- W. J. Handley, M. P. Hobson, and A. N. Lasenby. polychord: nested sampling for cosmology. *MNRAS*, 450:L61–L65, June 2015. doi: 10.1093/mnrasl/slv047.
- WJ Handley, MP Hobson, and AN Lasenby. Polychord: next-generation nested sampling. *Monthly Notices of the Royal Astronomical Society*, 453(4):4384–4398, 2015.
- Radford M. Neal. Slice sampling. *Ann. Statist.*, 31(3):705–767, 06 2003. doi: 10.1214/aos/1056562461. URL <https://doi.org/10.1214/aos/1056562461>.
- F. Feroz, M. P. Hobson, and M. Bridges. MULTINEST: an efficient and robust Bayesian inference tool for cosmology and particle physics. *MNRAS*, 398(4):1601–1614, October 2009. doi: 10.1111/j.1365-2966.2009.14548.x.
- Rupert Allison and Joanna Dunkley. Comparison of sampling techniques for bayesian parameter estimation. *Monthly Notices of the Royal Astronomical Society*, 437(4):3918–3928, 2014.
- John Veitch, Vivien Raymond, Benjamin Farr, W Farr, Philip Graff, Salvatore Vitale, Ben Aylott, Kent Blackburn, Nelson Christensen, Michael Coughlin, et al. Parameter estimation for compact binaries with ground-based gravitational-wave observations using the lalinference software library. *Physical Review D*, 91(4):042003, 2015.
- Ilias Cholis, Carmelo Evoli, Francesca Calore, Tim Linden, Christoph Weniger, and Dan Hooper. The galactic center gev excess from a series of leptonic cosmic-ray outbursts. *Journal of Cosmology and Astroparticle Physics*, 2015(12):005, 2015.
- Kazunori Akiyama, Antxon Alberdi, Walter Alef, Keiichi Asada, Rebecca Azulay, Anne-Kathrin Baczko, David Ball, Mislav Baloković, John Barrett, Dan Bintley, et al. First m87 event horizon telescope results. iv. imaging the central supermassive black hole. *The Astrophysical Journal Letters*, 875(1):L4, 2019.
- Joshua S. Speagle. DYNesty: a dynamic nested sampling package for estimating Bayesian posteriors and

evidences. *MNRAS*, 493(3):3132–3158, April 2020.
doi: 10.1093/mnras/staa278.

James Robert Lloyd, David Duvenaud, Roger Grosse, Joshua Tenenbaum, and Zoubin Ghahramani. Automatic construction and natural-language description of nonparametric regression models. In *Twenty-eighth AAAI conference on artificial intelligence*, 2014.

Shengyang Sun, Guodong Zhang, Chaoqi Wang, Wenyuan Zeng, Jiaman Li, and Roger Grosse. Differentiable compositional kernel learning for gaussian processes. *arXiv preprint arXiv:1806.04326*, 2018.

Jackson Loper, David Blei, John P. Cunningham, and Liam Paninski. General linear-time inference for gaussian processes on one dimension, 2020.